Light-dependent flavin redox and adduct states control the conformation and DNA-binding activity of the transcription factor EL222

Aditya S. Chaudhari[1,2,†], Adrien Favier [3,†], Zahra Aliakbar Tehrani[4,†], Tomáš Koval [5],
Inger Andersson[1,6], Bohdan Schneider [1], Jan Dohnálek[5], Jiří Černý [4], Bernhard Brutscher [3,*],
Gustavo Fuertes [1,*]

[1]Laboratory of Biomolecular Recognition, Institute of Biotechnology of the Czech Academy of Sciences, Vestec 25250, Czech Republic
[2]Faculty of Science, Charles University, Prague 11636, Czech Republic
[3]Université Grenoble Alpes, CEA, CNRS, Institut de Biologie Structurale (IBS), Grenoble Cedex 9, 38044, France
[4]Laboratory of Structural Bioinformatics of Proteins, Institute of Biotechnology of the Czech Academy of Sciences, Vestec 25250, Czech Republic
[5]Laboratory of Structure and Function of Biomolecules, Institute of Biotechnology of the Czech Academy of Sciences, Vestec 25250, Czech Republic
[6]Department of Cell and Molecular Biology, Uppsala University, Uppsala 75124, Sweden

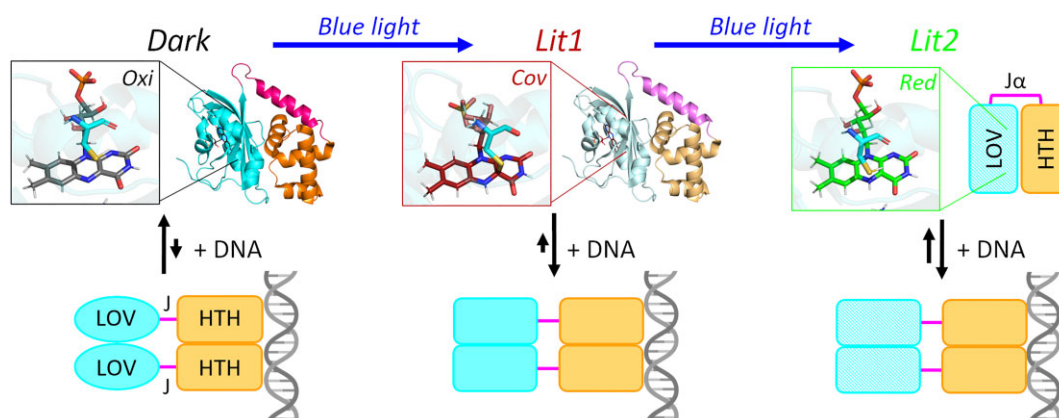*To whom correspondence should be addressed. Email: Gustavo.fuertes@ibt.cas.cz
Correspondence may also be addressed to Bernhard Brutscher. Email: bernhard.brutscher@ibs.fr
†Joint First Authors.

Abstract

The activity of the light-oxygen-voltage/helix-turn-helix (LOV–HTH) photoreceptor EL222 is regulated through protein–protein and protein–DNA interactions, both triggered by photo-excitation of its flavin mononucleotide (FMN) cofactor. To gain molecular-level insight into the photocycle of EL222, we applied complementary methods: macromolecular X-ray crystallography (MX), nuclear magnetic resonance (NMR) spectroscopy, optical spectroscopies (infrared and UV–visible), molecular dynamics/metadynamics (MD/metaD) simulations, and protein engineering using noncanonical amino acids. Kinetic experiments provided evidence for two distinct EL222 conformations (lit1 and lit2) that become sequentially populated under illumination. These two lit states were assigned to covalently bound N_5 protonated, and noncovalently bound hydroquinone forms of FMN, respectively. Only subtle structural differences were observed between the monomeric forms of all three EL222 species (dark, lit1, and lit2). While the dark state is largely monomeric, both lit states undergo monomer–dimer exchange. Furthermore, molecular modeling revealed differential dynamics and interdomain separation times arising from the three FMN states (oxidized, adduct, and reduced). Unexpectedly, all three EL222 species can associate with DNA, but only upon blue-light irradiation, a high population of stable complexes is obtained. Overall, we propose a model of EL222 activation where photoinduced changes in the FMN moiety shift the population equilibrium toward an open conformation that favors self-association and DNA-binding.

Graphical abstract

Introduction

Photoreceptors containing the light-oxygen-voltage (LOV) domain regulate multiple functions including phototropism in plants, the circadian clock in fungi, and stress response in bacteria [1–5]. Bacterial LOV proteins generally feature a simple organization where the LOV sensor domain is connected to an effector/output domain via a linker sequence [3]. This is the case of EL222, a transcription factor from the bacterium *Erythrobacter litoralis*, which contains an N-terminal sensory LOV domain and a C-terminal helix-turn-helix (HTH) DNA-binding domain [6]. EL222 is transcriptionally inactive in the dark but avidly binds to DNA and switches on gene expression upon illumination [6, 7]. Because of this property, EL222 has found widespread use in optogenetic applications that require rapid and reversible control of transcriptional activity [8–14]. The LOV core domain has a classical Per-Arnt-Sim (PAS) fold, consisting of a five-stranded antiparallel β-sheet and four helical elements, one of which holds a conserved cysteine residue (Cys78 in EL222). LOV signaling is dependent on a flavin chromophore, typically flavin mononucleotide (FMN), noncovalently bound in the dark state i.e. in the absence of light stimulation. A crystal structure of dark-state EL222 shows a canonical LOV fold tightly packed against the HTH domain ("closed" conformation) and a structurally heterogeneous linker that is partially invisible, most likely disordered, and partially α-helical (Jα element) [6]. High-resolution structure(s) of light-activated EL222 have so far been missing.

The hallmark of LOV domain photochemistry is the formation of a FMN–cysteinyl adduct, which features both a conserved cysteine residue covalently bound to the C4a atom of the FMN moiety (responsible for a shift in the absorption maximum from 450 to ~390 nm), and protonation of the N_5 atom of FMN [4, 5]. Fold-switching has been proposed for EL222 with the lit state being more disordered than the dark state [15]. Moreover, EL222 is mostly monomeric in the absence of illumination, while upon illumination it forms transient dimers that may be stabilized in the presence of DNA [16–18]. After ceasing illumination, EL222 returns spontaneously (thermally) to the dark-state configuration in a timescale of seconds [15, 19].

In summary, according to the current model of EL222 photocycle, dark-state "closed" (LOV–HTH interactions) monomers switch to an "open" (absence of LOV–HTH interactions) monomeric adduct state that is primed for dimerization through LOV–LOV and/or HTH–HTH interactions [6, 15]. Given the complex interplay between secondary, tertiary and quaternary structural changes in EL222 and the limited information gathered so far, the current model is, most likely, oversimplified.

In order to gain more insight into the structural and dynamical changes of EL222 upon illumination, both with respect to the protein chain and the FMN chromophore, we undertook an integrative approach combining macromolecular crystallography (MX), solution nuclear magnetic resonance (NMR) spectroscopy, UV–visible and infrared (IR) spectroscopy, and molecular dynamics (MD) simulations. Importantly, all these techniques can be applied not only in the absence but also in the presence of continuous illumination, hence enabling access to photostationary conditions and minimizing sparsely populated transient species arising from pulsed illumination.

Materials and methods

Protein and DNA preparation

Five versions of EL222 were prepared (see Supplementary Table S1). Most studies employed the EL222 (17–225) variant (following UniprotKB Q2NB98) numbering, which differs from PDB numbering by an interval of -3. This is a quasi-full-length variant, referred to as EL222–WT, lacking part of the disordered N-terminus known to promote protein instability [6]. We also prepared a mutant lacking the conserved cysteine (EL222–C78A) [20], a slow recovery quadruple mutant (EL222–AQTRIP) [18], and a variant with a noncanonical 4-cyano-L-phenylalanine (pCNF) residue at position 31 (EL222–W31pCNF) by genetic code expansion [15]. We also prepared a shorter version, EL222–LOV containing only the LOV domain, i.e. lacking the linker and HTH domains. The purification tags were removed as previously described for EL222(17–225) [15]. The final proteins contain only native residues except for the C-terminal alanine "scar" and the GEF sequence at the N-terminus of EL222-LOV. All protein handling steps were done under dim light. Proteins were flashed-frozen in liquid nitrogen and stored at −80°C until used.

Forward and reverse DNA oligonucleotides (Supplementary Table S1) were purchased separately (Sigma), dissolved in MES 50 mM, pH 6.8, NaCl 100 mM, mixed in equimolar ratios and annealed by first heating up to 95°C and then cooling down to room temperature (1°C/min). The resulting double-stranded DNA was kept at 4°C and used within one week.

Mass spectrometry

All proteins were analyzed by mass spectrometry to determine the molecular weight. Proteins were diluted with 100 μl of 5% acetic acid in water and loaded onto Opti-trap C4 cartridge (Optimize Technologies), washed 4× with 250 μl of 5% acetic acid in water, and eluted with 100 μl of 80% acetonitrile and 5% acetic acid. Proteins were analyzed by direct infusion using syringe pump at a flow rate 2 μl/min connected with an electrospray ion source of 15 T solariX XR FT-ICR mass spectrometer (Bruker Daltonics). The mass spectrometer was externally calibrated using 1% (w/w) sodium trifluoracetate. Proteins were measured in positive mode with 2 M data acquisition. The data were processed using SNAP algorithm, a part of DataAnalysis 4.4 software (Bruker Daltonics).

To determine post-translational modifications in the EL222-WT batch used crystallization, the protein was digested using trypsin and further analyzed by LC-MS/MS using a timeToF Pro mass spectrometer (Bruker, Germany).

NMR spectroscopy

All NMR experiments were performed at 25°C on Bruker Avance III HD spectrometers (700, 850, or 950 MHz ^{1}H frequency) equipped with helium-cooled triple-resonance probes (HCN TCI 5 mm) and pulsed z-field gradient. EL222 samples were prepared as 300 μl of protein solutions at 200 μM concentration (unless otherwise stated) dissolved in 25 mM MES buffer, pH 6.8, 50 mM NaCl (plus the addition of 5% deuterium oxide). To increase sample stability over long time periods, 3 μl of a cOmplete protease inhibitor cocktail (Roche Applied Science) was added. Samples were placed in NMR Shigemi tubes of 2 cm length and 5 mm diameter. ^{1}H–^{15}N correlation spec-

tra and 3D NMR experiments for backbone assignments (HNCO, HNCACO, HNCA, and HNCOCA) were obtained using Band-selective Excitation Short-Transient Transverse Relaxation-Optimized Spectroscopy (BEST-TROSY) [21] correlation experiments, as implemented in the NMRlib sequence library package [22], which can be freely downloaded from the IBS website (http://www.ibs.fr/research/scientific-output/software/pulse-sequence-tools). Customized H(N)C, H(NCO)N, and H(N)CO experiments were used for NMR resonance assignments of the FMN moiety in the different photostationary states. Translational diffusion of the protein and protein:DNA complexes in solution were measured by 1D ^{1}H Diffusion Ordered Spectroscopy (DOSY) experiments [23]. Focusing on the amide or methyl ^{1}H spectral regions, a series of 1D spectra were recorded with varying gradient strength and a total acquisition time of ~20 min. ^{15}N T$_2$ transverse relaxation experiments were performed on uniformly ^{15}N–^{13}C-labeled protein samples using standard NMR pulse sequences [24]. The NMR signal decay was sampled for 10 relaxation time points varying between 0 and 128 ms. The rotational diffusion constants of proteins and protein/DNA complexes, related to their particle size, has been determined by TRACT experiments [25], which measures the relaxation rate difference of the two doublet components of a ^{1}H-coupled ^{15}N (amide group) in a series of 1D ^{1}H experiments.

The recorded NMR data were processed and analyzed using Bruker Topspin 3.5 and CCPNMR V2 software (Collaborative Computing Project for NMR; https://ccpn.ac.uk/software/version-2/version-2-downloads/).

In situ NMR sample illumination has been achieved as described previously [26]. A laser source of a typical power of 70 mW, emitting maximally at 488 nm, was used to photoconvert the samples. This corresponds approximately to a power density of 260 mW/cm^2 at the top of the NMR sample tube.

IR spectroscopy

Steady-state infrared spectra of EL222 variants were measured with a Bruker Vertex 70v FTIR (Fourier-transform infrared) spectrometer equipped with a globar source, KBr beamsplitter, and a liquid nitrogen cooled mercury cadmium telluride (MCT) detector. The protein samples in MES 50 mM, NaCl 100 mM, pH 6.8 were centrifuged at 18 000 *g* for 15 min to remove any precipitants before measurements. For measurements in the Amide I band (EL222–WT and EL222–C78A samples), D$_2$O was employed, while for measurements in the "transparent window" (sulfhydryl band of EL222–WT and EL222–C78A, and nitrile band of EL222–W31pCNF), H$_2$O buffer was utilized instead. D$_2$O buffer exchange was done by a centrifugal concentration method using 10 kDa cutoff filters. The aperture value was set in order to get maximum signal without saturating the detector. Approximately 25 μl of sample was loaded into a temperature controllable demountable liquid cell with CaF$_2$ windows and a 50-μm Teflon spacer. Eighteen spectra were recorded at 20°C and 15-min intervals. The initial 14 spectra were recorded while the protein was illuminated to induce the lit state, achieved using two LEDs emitting a power of 100 mW/cm^2 onto the sample throughout the measurement. The final four measurements were taken with the lights turned off. All difference spectra were recorded against the initial spectra in the absence of illumination (dark state). The double difference spectra of Fig. 6C were calculated as (lit$_x$-dark)^{DNA} minus (lit$_x$-dark)^{free}, where the subindex$_x$

can be 1 or 2, and DNA/free denotes the presence or absence of DNA, respectively. Protein samples had concentrations between 0.5 and 1 mM. In the case of protein–DNA mixtures equimolar ratios were employed. A water vapor spectrum was measured with the same parameters and utilized to remove any water vapor contamination present in the obtained protein spectra. The spectra underwent baseline correction using OriginPro (OriginLab). The analysis of the kinetic traces is reported in the Supplementary Information.

UV–visible spectroscopy

The UV–visible absorbance spectra of the EL222 protein within the 320–550 nm range were obtained using a Specord 50 Plus spectrometer (Analytik Jena). Measurements were conducted at 20°C in a quartz cuvette (Hellma Analytics) with a 10-mm path length for quantification purposes and a 1-mm path length for lit state induced measurements, with sample volumes of 70 and 600 μl, respectively. To ensure an airtight environment for lit state measurements, the cuvette opening was sealed with a PTFE lid and parafilm. Prior to dark state sample measurements, MES buffer served as the background measurement. The protein's lit state was induced by 3 h of continuous illumination using three 455-nm LED with a power of 1 mW/mm^2, covering the entire cuvette. Subsequently, the LEDs were deactivated, and spectra were recorded.

X-ray crystallography

EL222–WT was crystallized at 18°C and a concentration of 10 mg/ml using the sitting drop vapor diffusion setup with a reservoir solution containing 0.11 M MES, pH 6.5, 0.22 M MgCl$_2$, and 21% (w/v) PEG 8000. Crystals of EL222dark and EL222light were retrieved from the same drop, mounted on the diffractometer under a stream of air of 96% relative humidity at room temperature, conditioned for 30 min, and then vitrified in a cold nitrogen gas stream (100 K). All manipulation of the EL222dark crystal was done under low ambient light. The EL222light crystal was illuminated, using a 470 nm LED light source, during conditioning and data collection. X-ray diffraction data were collected at 100 K using a D8 Venture diffractometer. Phases were obtained by molecular replacement using PDB ID 3P7N as a template, and the structures were manually built/modified and refined. FMN in the lit1 state in EL222light was modeled covalently bound to Cys78 with 30% occupancy. Statistics for data collection, processing, and refinement are reported in Supplementary Table S2. A detailed description of all experimental procedures is reported in the Supporting Information.

Molecular modeling simulations

Classical MD simulations were employed to study conformational changes and dynamic behaviors of the FMN–EL222 complex in both dark (oxi^{MD}) and lit1/lit2 (cov^{MD}/red^{MD}) states. Initial models were derived from X-ray structures (PDB codes: 8A5R and 8A5S) using a periodic dodecahedron simulation box extending the solute size by 1 nm in all directions filled with the TIP3P water. The sodium and chloride ions were added reaching a charge-neutral system with 100 mM salt concentration. The MD force field parameters for covalently and noncovalently bound FMNs were generated using the standard RESP fitting procedure [27, 28]. The simulations consisted of a minimization step using the steepest descent algorithm. The minimization was performed within

up to 50 000 steps with a maximum step size of 0.01 nm and convergence limit of 500 kJ/mol/nm. Following the minimization step, a short equilibration was conducted under the NVT conditions (constant particle number, volume, and temperature) using a V-rescale modified Berendsen thermostat at 300 K, which consisted of 50 000 steps with a time step of 2 fs. The equilibration then continued at 300 K and 1 bar under the NPT ensemble conditions with a Parrinello-Rahman barostat. The pressure equilibration phase involved 50 000 steps with a time step of 2 fs, and both short-range Coulomb and van der Waals (vdW) cutoffs set to 1 nm, while the long-range electrostatics was treated by Particle Mesh Ewald (PME) [29, 30]. The production simulations for the oxi^{MD}, cov^{MD}, and red^{MD} states included three independent MD replicas under the same NPT conditions, each lasting 1 ms, collecting 3 ms of cumulative MD data for each simulated system. Since light-oxygen-voltage/helix-turn-helix (LOV–HTH) domain separation has not been observed within the time scale of these classical MD simulations, metadynamics simulations (metaD) were employed as an alternative approach to explore the relative behavior of oxi^{metaD}, cov^{metaD}, and red^{metaD} states in terms of LOV–HTH domain separation. The MD and metaD simulations were performed using the GROMACS package version 2023.2 [31, 32] extended by the PLUMED version 2.10.0_dev [33, 34]. Details of the MD and metaD simulation parameters reported in this study are provided in the Supporting Information.

Results

EL222 crystal structures support adduct formation

We first determined the crystal structures of EL222 in the dark (PDB ID: 8A5R) and lit (PDB ID: 8A5S, under 470 nm illumination) states, both at 1.85 Å resolution, from crystals retrieved from the same crystallization hanging drop (Supplementary Table S2). The overall fold closely resembles the structure determined previously (PDB ID: 3P7N [6]; Supplementary Table S3) showing the N-terminal LOV and C-terminal HTH domains connected by the long Jα helix (Fig. 1A). Both the dark and the lit structures are supported by continuous electron density for residues T21–A226. In addition, an N-terminal segment (residues 21–27), the C-terminal non-native residue A226, and a segment comprising residues 145–152, all absent in the previously published structure (PDB ID: 3P7N[6]) could be modeled in our electron density maps. Residues 145–149 precede the Jα helix and presumably serve as a hinge enabling relative movements of the LOV and HTH domains as part of the signaling cycle. The HTH domain fixes the position of the Jα helix in an extended conformation, hindering Jα to dock onto the LOV domain β-sheet as observed in the structures lacking the HTH domain [5]. Both structures contain oxidized histidine (2-oxo-histidine) at position 101, presumably because of oxidative stress. This modification, confirmed by mass spectrometry (Supplementary Fig. S1) was present in EL222 prior to crystallization, likely being caused by inadvertent light or redox activation of the protein during expression and purification.

In both states, FMN binding to the LOV domain of EL222 is similar to previous reports [5, 6] orienting the isoalloxazine C4a atom close to the Cys78S$^\gamma$. In the dark, the C4a-S$^\gamma$ distance refines to 3.4 Å. Under illumination, electron density around FMN indicates the presence of two popula-

tions; one is very similar to our dark state model (C4a-S$^\gamma$ distance 3.3 Å, Fig. 1C). In the second population, the distance is shortened to 1.8 Å, suggesting the presence of a covalent bond (Fig. 1B). As a result, the C4a atom is sp3 hybridized, which in turn results in puckering of FMN around the C4a atom (Fig. 1B). The occupancies of the noncovalent/covalent (adduct) states of FMN in the illuminated crystals are estimated to be 70%/30%, respectively. Thus, we consider that, under our illumination conditions, 70% of the molecules in the crystal remained in the dark state and 30% were photoconverted. The arrangement of domains is very similar in the dark and lit models (Fig. 1A). A close inspection reveals a small, but distinguishable, shift of the HTH domain with the largest changes observed in the loop between the 1α and 2α helices, most of the 3α helix and at the beginning of helix 4α (Supplementary Fig. S2A and Supplementary Table S3). Changes in the positions of atoms in the vicinity of Gln141 (Leu138–Ser140) propagate further along the LOV–HTH interface ultimately changing the mutual orientation of contacts between LOV and HTH domains (Supplementary Fig. S2B).

The structural changes observed upon illumination of the crystals clearly indicate the progression of short-range atomic shifts following the formation of the FMN–Cys covalent bond. Such shifts may be the precursor to long-range conformational changes (domain separation and oligomerization). However, the latter may not occur in the whole crystal given the restrictions imposed by the crystal lattice. Thus, we next probed the light-induced structural and dynamical changes of EL222 by solution spectroscopy techniques.

EL222 photocycle in solution is characterized by three conformational states

First, we applied solution NMR spectroscopy on uniformly ^{13}C–^{15}N-labeled EL222 samples. Upon illumination with blue light (488 nm), we observed significant changes in the amide ^{1}H–^{15}N correlation spectra (Fig. 2A). Notably, in addition to the dark-state species (colored black in Fig. 2A), two lit-state populations, characterized by a distinct set of resonances, were observed and named lit1 (colored red in Fig. 2A) and lit2 (colored green in Fig. 2A). The NMR spectral signature characteristic of lit1 is detected after <1 min of blue-light illumination, while lit1 then slowly photoconverts into lit2 on a timescale of hours (Supplementary Fig. S3A) under continuous illumination. The kinetic rate of the lit1-to-lit2 conversion increased linearly with the applied light power (Supplementary Fig. S3C and Supplementary Table S4) indicative of a single-photon photochemical process. The kinetics were also faster in the presence of ascorbate (Supplementary Fig. S3D) indicative of a photoinduced electron transfer reaction. In the absence of light, the lit1 state reverted quickly back to the dark-state conformation, in agreement with the reported dark recovery lifetime of FMN in EL222 (~40 s at pH 6.8 and 20°C) [15]. When turning off the light, after having photoconverted EL222 to the lit2 state, samples remained largely transparent and the characteristic yellow color of oxidized FMN was not restored (*vide infra*). In addition, the NMR spectral signature did not change over time, indicating that lit2 is not spontaneously back-converting, neither to the lit1 nor to the dark state in our experimental conditions. Restoring the dark state required opening the NMR (Shigemi) tube (Supplementary Video S1). We rationalize these observations by the requirement of molecular oxygen for the conver-
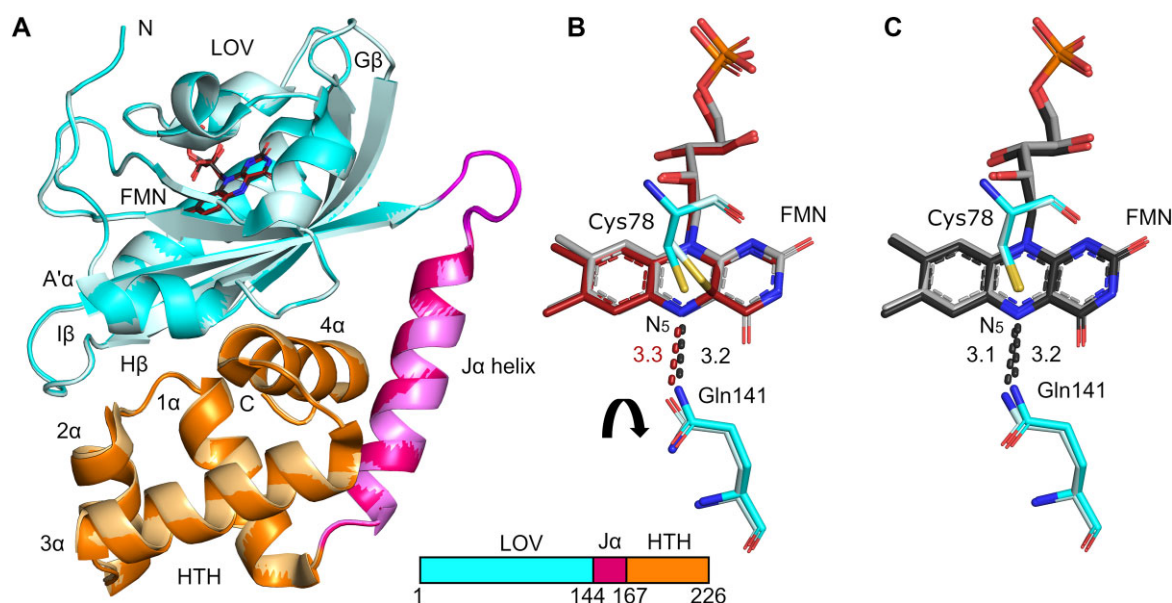
Figure 1. X-ray crystallography studies of EL222 show evidence for adduct formation upon illumination. Superposition of EL222 structures crystallized and measured in the dark (PDB ID: 8A5R or "dark" structure, one species) or with continuous blue light illumination (PDB ID: 8A5S or "lit" structure, containing two species). (**A**) Cartoon representation of complete EL222. (**B** and **C**) Details of FMN chromophore binding in stick representation, shown as alignment of (B) FMN from "dark" structure with FMN from "lit" structure in covalently bound state (30% partial occupancy), and (**C**) FMN from "dark" structure with FMN from "lit" structure noncovalently bound (70% partial occupancy). Residues C78 and Q141 are also shown as sticks. Hydrogen bonds of Gln141Nε2 to FMN-N_5 in the dark and dark-like structures are shown as dashed lines. The hydrogen bond between Gln141Oε1 and FMN-N_5 in the adduct state is also shown as a dashed line. All distances are given in Å. The rectangular inset represents the domain structure of EL222. Molecular graphics were created using PyMOL (Schrödinger, LLC).

sion from lit2 to the dark state of EL222. In the NMR tube, the water-dissolved oxygen may become depleted during the photoconversion from lit1 to lit2 states due to photoinduced electron transfer, leaving no oxidant for the back conversion to the dark state.

The observed ^{1}H–^{15}N chemical shift changes between the dark and the lit1 or lit2 states are mainly localized to the LOV domain (Supplementary Fig. S4), suggesting that light-induced chemical and structural changes are sensed primarily by nuclei in the vicinity of the FMN cofactor. We therefore investigated the role of the additional HTH domain in this photocycle by repeating the NMR photoconversion experiment on the isolated LOV domain embedding the FMN cofactor. The same three photo-states (dark, lit1, and lit2) were observed for this construct (Supplementary Fig. S5A), although with a 10-fold increase of the lit1-to-lit2 conversion rate (Supplementary Fig. S3B). This suggests that the lit2 state may be a general property of LOV domains, while the effector (DNA binding) domain significantly slows down the conformational transition from lit1 to lit2. Previous NMR studies of a slightly different variant of EL222 assigned the ^{1}H, ^{13}C, and ^{15}N chemical shifts in the dark state (BMRB 17640) but identified only one species upon illumination [6]. By comparing the patterns in chemical shift differences (Supplementary Fig. S4A and B), we conclude that our EL222 lit1 state corresponds to the previous lit state.

To understand the nature of these two states (lit1 and lit2), we examined the redox state of the FMN moiety. Isolated FMN can undergo two successive electron reductions (eventually accompanied by proton transfer) to form either a semiquinone radical or a hydroquinone form (Supplementary Fig. S6). While the flavin N_3 is protonated in all three species, N_1 only becomes protonated in the hydroquinone

form at low pH, and N_5 is expected to be protonated in semiquinone and hydroquinone FMN [35]. Therefore, these different chemical species can be distinguished by NMR observation of their characteristic ^{1}H–^{15}N spectral signatures [36–38]. NMR data recorded on EL222 in its different photo-states (Supplementary Fig. S7A) are in agreement with FMN being oxidized in the dark, N_5 protonated in lit1, and with all FMN nitrogens (N_1, N_3, and N_5) protonated at pH 5.5 in lit2.

To investigate whether an FMN–cysteinyl adduct is formed in the two lit states, we combined NMR, infrared and UV–visible spectroscopy data. The ^{13}C chemical shift of the FMN C4a carbon is a sensitive reporter of this adduct formation with a value of about 135 ppm for free FMN and 65 ppm if FMN is forming a covalent bond between the C4a and the sulfur atom of a nearby cysteine side-chain [37]. The 2D H3(N3)C correlation spectrum, shown in Supplementary Fig. S7B, provides an indirect measure of this NMR chemical shift with an expected H3–C4a peak doublet if no adduct is formed, and a singlet peak in case of adduct formation. These NMR data show that the chemical bond with C4a is only formed in the lit1 state. The absence of adduct formation in lit2 is further confirmed from NMR data recorded for an EL222–C78A mutant lacking the conserved cysteine that engages in covalent bond formation with the FMN. No evidence of lit1 state formation was found for this mutant, and the dark state converted rapidly to the lit2 state upon illumination (Supplementary Fig. S5B). The same conclusion was obtained from infrared difference spectra recorded on EL222 under dark and light conditions using the SH stretching band ($\sim$2570 cm^{-1}) as a "transparent window" vibrational reporter [39, 40]. The lit-minus-dark state spectrum after short irradiation, corresponding to the lit1 state, showed a negative band suggesting the disappearance of sulfhydryl bonds and their
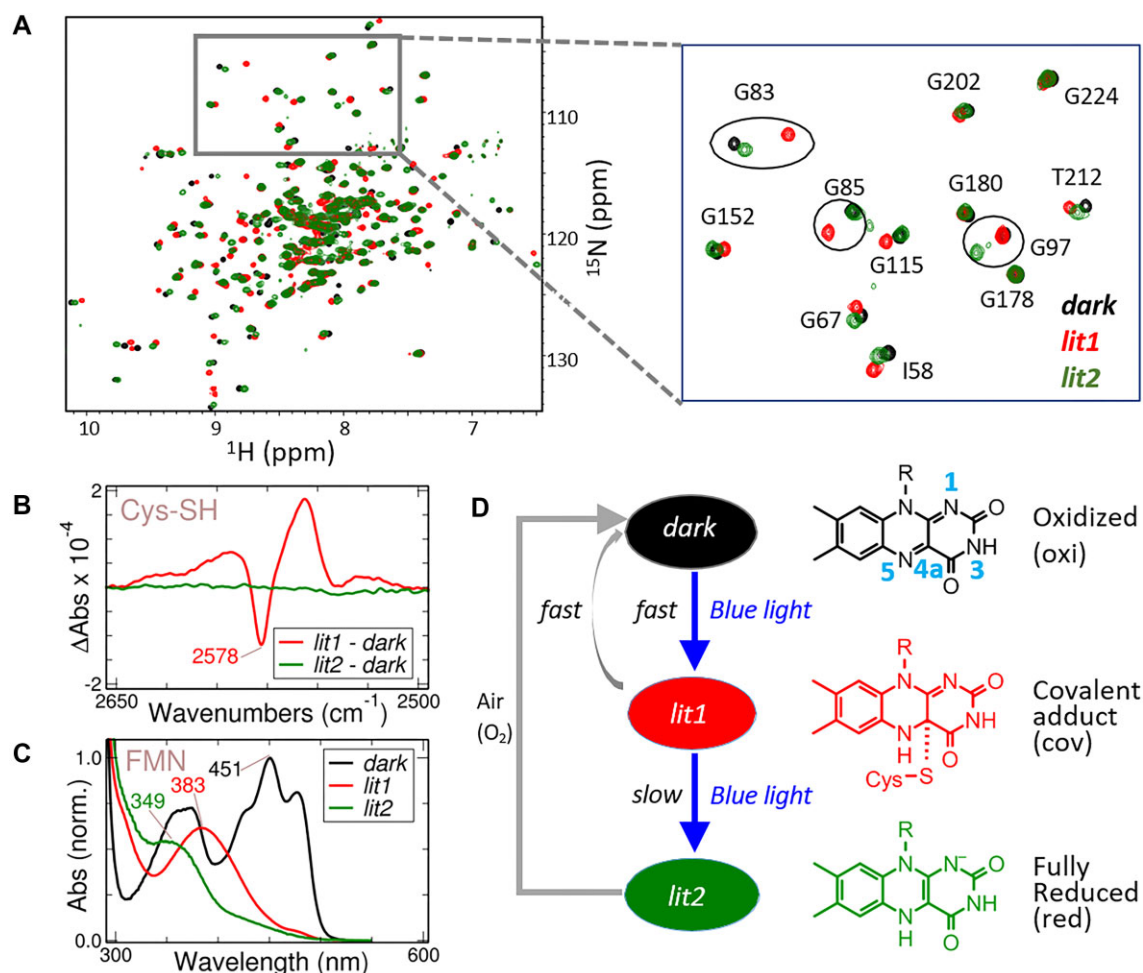
Figure 2. Solution spectroscopy reveals three distinct EL222 conformational states differing in the FMN redox state and adduct formation. (**A**) Superposition of ^{1}H–^{15}N correlation spectra of EL222 acquired in the dark, and after short and prolonged blue-light illumination. Right, small spectral region highlighting the observed chemical shift differences, indicative of changes in the electronic environment of a particular nuclear site. The observed NMR signatures (correlation peaks) correspond to pure dark, lit1, and lit2 states. (**B**) Species-associated infrared difference spectra in the sulfhydryl stretching region of EL222. (**C**) UV–visible absorbance spectra of EL222 in dark, lit1, and lit2 states. (**D**) Proposed model of EL222 photocycle. In the absence of illumination, the dark state conformation with oxidized FMN prevails. Under constant illumination, two species are formed sequentially. The lit1 state (FMN–cysteinyl adduct with N_5 protonated), which forms rapidly under blue-light irradiation, slowly (hours) converts into the lit2 state featuring fully reduced and noncovalently bound FMN. Contrary to the lit1 state, which swiftly (seconds' time scale) reverts back to the dark state conformer upon ceasing illumination, the lit2 state is a new species that does not relax spontaneously (thermally) in the absence of oxygen.

replacement by thioether bonds vibrating elsewhere (Fig. 2B). Interestingly, the difference spectrum after prolonged irradiation was nearly zero indicating that sulfhydryl groups are restored, i.e. the adduct is broken, in the lit2 state (Fig. 2C). IR difference spectra acquired for EL222–C78A in the amide I' band showed evidence of only one lit state with minor changes in SH bond vibrations (Supplementary Figs S8 and S9).

Finally, we recorded UV–visible spectra, which are well-known markers of FMN redox state and thioadduct formation [41]. We also measured an EL222 mutant, named AQTrip, that has a significantly lengthened lifetime of the lit1 state in the absence of illumination [18], thus allowing us to record a UV–visible absorption spectrum of this metastable state (Fig. 2C and Supplementary Fig. S10). The absorption band around 390 nm characteristic of chemical bond formation is only visible for lit1, and the decoloring of FMN is apparent from the spectrum of lit2.

Our observations in solution can be summarized in an extended photocycle of EL222 that is depicted in Fig. 2D. In the

absence of blue-light illumination, oxidized FMN (*oxi* FMN state), noncovalently bound to EL222, is the dominant species (corresponding to the crystal structure in the dark). Under illumination conditions, the lit1 state, which features FMN covalently bound to Cys78 and protonated at the N_5 position (*cov* FMN state), fully reverts to the dark state in the absence of illumination. The 30% of molecules in the illuminated crystals containing an adduct most likely correspond to the lit1 state. Prolonged illumination in the absence of oxygen or illumination of EL222 variants lacking the reactive cysteine leads to the irreversible formation of lit2, which is characterized by noncovalently bound FMN in the fully (two-electron) reduced state (*red* FMN state). Due to the combined requirement of high irradiances and anaerobiosis, the lit2 state is not expected to be an abundant intermediate in the photocycle of many LOV photosensors. However, the discovery of LOV receptors lacking the photoactive cysteine [42] raises the possibility that the lit2 state may play a physiological role in certain organisms and environments.

Structural and oligomerization properties of the three EL222 states

To obtain additional site-specific information about EL222 conformation and dynamics, we first performed NMR backbone ^1H, ^{15}N, ^{13}CO, and ^{13}CA chemical shift assignments of the dark (BMRB 52621) and lit2 (BMRB 52622) states that remain stable for several days allowing the recording of a series of 3D H-N-C correlation spectra. In addition, partial ($\sim$70%) ^1H, ^{15}N assignments were obtained for the transiently formed lit1 state (BMRB 52620). Note that our dark state NMR chemical shifts closely match those reported in [6] for a similar EL222 construct (BMRB 17640). These chemical shifts report on the local electronic environment of a nucleus, and therefore only indirectly on the molecular structure. ^1H-^{15}N chemical shift differences between the dark and lit1 or lit2 states are mainly localized in the FMN-containing LOV domain (Supplementary Fig. S4). Backbone ^{13}C chemical shifts provide sensitive reporters on secondary structural elements along the peptide sequence [43, 44]. Chemical-shift based TALOS predictions [45, 46] of secondary structure propensities in EL222 are in good agreement with the structures presented here and with the previously determined crystal structure (3P7N) [6], and no significant changes in secondary structure are observed upon prolonged blue light illumination (lit2) (Supplementary Fig. S11). Furthermore, ^{15}N transverse relaxation times (T_2) measured for individual backbone amides along the peptide sequence in the three photostationary states indicate that monomeric EL222 forms a compact protein structure in all states (Fig. 3A). No indication of additional local dynamics or segmental motion of the individual protein domains upon illumination is obtained from these data. The rotational tumbling correlation times extracted from the measured ^{15}N T_2 and additional TRACT data (Supplementary Fig. S12) are very similar for the dark and lit states, and in agreement with monomeric EL222 particles in solution. However, these results do not exclude the possibility of EL222 dynamics occurring on longer time scales.

IR difference spectra in the structure-sensitive amide I' band (1600–1700 cm^{-1}), mainly reporting on the C=O stretching vibrations of the protein backbone [47], suggest that the two light-induced conformational states of EL222 differ in their secondary structure content (Fig. 3C right; Supplementary Fig. S9 and Supplementary Table S4). While the lit1 state shows a loss of α-helical content with respect to the dark state (negative band at 1647 cm^{-1}), as previously reported [15], no such drop of α-helicity is detected for the lit2 state. Moreover, the negative/positive bands at 1673 cm^{-1}/1622 cm^{-1}, which may be tentatively assigned to β-sheets, suggest that the secondary structure content of lit2 is different from the dark state. This apparent discrepancy between NMR (no major secondary structure changes) and IR data (distinct secondary structure in dark, lit1, and lit2 states) can be reconciled considering a model where monomeric EL222 is in slow exchange (rate constant < 100 s^{-1}) with oligomeric species. While EL222 dimers, and higher-order oligomers, are essentially NMR-invisible under our experimental conditions, IR is sensitive to all species present in solution regardless of their size. Thus, photoinduced secondary structure changes seem to occur preferentially in oligomeric EL222 species.

To further investigate potential differences in oligomerization propensity between the dark and lit states of EL222, we have performed additional NMR and IR experiments. As oligomerization is a concentration-dependent process, we expect that more oligomers are formed at higher protein concentration. With the hypothesis of a slow exchange process, we expect the intensity of NMR signals arising from monomeric EL222 species to be reduced at higher EL222 concentrations. The peak intensity ratios measured in ^1H–^{15}N spectra after 4-fold protein dilution are plotted in Fig. 3B. While in the dark no significant change in peak intensities is observed, the relative peak intensity increases upon dilution for both the lit1 and lit2 states, indicative of the presence of oligomeric species. For IR spectroscopy, we employed an EL222 variant carrying the noncanonical amino acid pCNF at position 31. This variant was previously shown to report on the monomer–multimer equilibrium via a red-shift (the nitrile band of oligomeric species vibrating at lower frequency than the monomers) [15]. The IR difference spectra of EL222–W31pCNF in the C≡N stretching region are similar for lit1 and lit2 states (Fig. 3C left; Supplementary Fig. S9 and Supplementary Table S4) again suggesting the presence of oligomers in both cases. The smaller spectral amplitudes of the lit2 state may be compatible with a lower population of oligomers relative to lit1. These observations support a model (Fig. 3D) where, in the presence of blue light, monomeric EL222 is in slow exchange with oligomeric species, most likely due to interaction of EL222 molecules in an "open" conformation, where the LOV domain is no longer protected by the HTH domain from binding to another LOV domain. The exact stoichiometry of the EL222 oligomers is unknown with dimers [7, 16–18] and higher-order oligomers being described in the literature, the latter only in the absence of DNA [48]. This model is consistent with photoinduced tertiary structure changes in EL222 observed earlier by hydrogen–deuterium exchange and proteolysis susceptibility experiments [6].

Molecular modeling indicates FMN-dependent dynamics of EL222

To gain deeper insights into the structural dynamics of EL222, a series of MD simulations were conducted (see details in Supplementary Information). All-atom molecular models of EL222 were created featuring FMN in its *oxi*, *cov*, and *red* states (Fig. 4A), intended to reproduce the properties of the experimentally determined dark, lit1, and lit2 states, respectively. Specifically, the *oxi* model contains oxidized FMN noncovalently bound to EL222; the *cov* model features FMN covalently bound to the Cys78 residue, with a hydrogen at position N_5 (N_5H), and a 180° rotated Gln141 residue; and the *red* model represents fully reduced, negatively charged FMN (N_5H/N_1^-) noncovalently bound to EL222 (Fig. 4A and Supplementary Table S5).

Employing Root Mean Square Fluctuation (RMSF) analysis, which evaluates the average displacement of atomic positions relative to their mean positions throughout the MD simulation, we systematically investigated flexible and rigid structural regions, including α-helices and β-strands, within the EL222 protein. The differential RMSF (ΔRMSF) profiles of all Cα atoms of EL222 protein residues in cov^{MD} and red^{MD} simulations, relative to oxi^{MD}, are depicted in Fig. 4B (individual RMSF plots can be found in Supplementary Fig. S13). Most regions of EL222 have low ΔRMSF values, indicating that the protein remains quite stable, regardless of the FMN state. The N-terminal residues exhibit the most pronounced
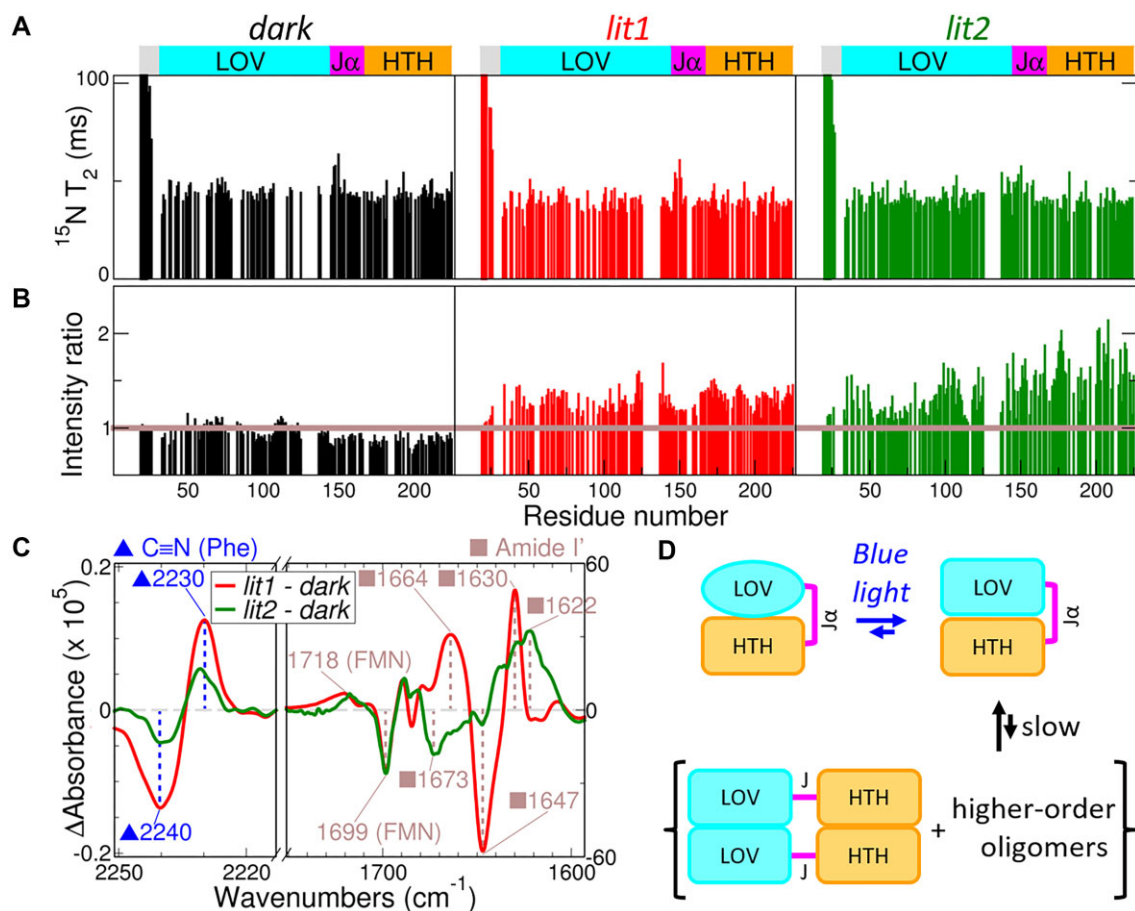
Figure 3. The three conformational states of EL222 differ in oligomerization propensity. (**A**) Residue-specific transverse ^{15}N backbone relaxation times (T_2) plotted as a function of the EL222 sequence for the dark (left), lit1 (middle), and lit2 (right) states. (**B**) NMR intensity ratios of the different states plotted as a function of residue number upon 4-fold EL222 dilution from 120 to 30 μM. (**C**) Species-associated infrared difference spectra in the nitrile (C≡N) stretching region of EL222-W31pCNF (left) and in the amide I′ (C=O) region of EL222-WT (right) support the presence of two conformational states under continuous illumination differing in oligomerization and secondary structure content. (**D**) Model of photoinduced conformational changes of EL222 in the absence of DNA: Blue light promotes EL222 oligomerization, including dimers and higher-order oligomers. The fraction of molecules that remain monomeric show virtually no secondary structural changes with respect to the dark state. Only some residues in EL222 oligomers (NMR-invisible) undergo helix-to-coil transition, most likely in the connecting element between the LOV and HTH domains (so-called Jα in the dark state, here renamed as J in the lit states); pCNF, *para*-cyano-L-phenylalanine (noncanonical amino acid).

variations of RMSF in cov^{MD} and red^{MD} trajectories compared to oxi^{MD}. Enhanced RMSF and flexibility relative to oxi^{MD} are observed in the Iβ-Jα loop and the N-terminal part of Jα-helix (residues Asp147-Arg155) of the cov^{MD} simulations. This might indicate a conformational change or increased flexibility due to covalent bond formation in the LOV domain. We have included the B-factors derived from the experimental X-ray structures in Supplementary Fig. S13, alongside the RMSF profiles from MD simulations (oxi^{MD}, cov^{MD}, and red^{MD} states). This addition highlights the good agreement between the experimental crystallographic and computational MD data.

Although these results offer valuable insights into the dynamics of EL222, our classical MD simulations do not provide information on the key photoinduced processes, such as the detachment/unfolding of the Jα-helix region or domain rearrangements [49]. To explore the dissociation of LOV and HTH domains in EL222, we employed metadynamics (metaD) simulations [33, 50, 51] of the three molecular models (oxi, cov, and red, Fig. 4A) by applying a biased potential along an inter-domain distance that consequently induces par-

tial disordering of Jα (Fig. 4C, see SI for more technical information). The time when this applied force effectively caused inter-domain separation was collected for oxi^{metaD}, cov^{metaD}, and red^{metaD} (Supplementary Fig. S14A). The histograms of simulated LOV-HTH domain separation times for EL222 reveal significant differences among the various FMN states (Supplementary Fig. S14B). It should be noted here that the metadynamics simulations were not intended to yield absolute kinetic values (comparable to the multi-microseconds separation times) but rather to reveal differences between the three EL222 states. Thus, to facilitate such comparisons, the inter-domain separation times have been normalized relative to the oxidized state (oxi^{metaD}) (Fig. 4D). The covalent state (cov^{metaD}) shows a shorter relative mode separation time of 0.75, indicating that adduct formation and protonation at FMN-N_5 accelerate domain separation. The reduced N_1^- state (red^{metaD}) has an intermediate relative mode time of 0.93, falling between between oxi^{metaD} and cov^{metaD}. The marked decrease of LOV-HTH separation times in cov^{metaD} (Fig. 4D) supports the view that the covalent modification plays a key mechanistic role in EL222 domain separation.

In addition to inter-domain separation times, the maximum bias values required for LOV–HTH separation were extracted from each metaD simulation replica of EL222 in the oxi^{metaD}, cov^{metaD}, and red^{metaD} states (Supplementary Fig. S14C, technical details in Supplementary Information). The same mode-normalized approach was applied for the maximum bias values relative to the oxidized state and visualized using kernel density estimation (Supplementary Fig. S14D). These relative maximum bias values complement our analysis of LOV–HTH domain separation times (Fig. 4D). The cov^{metaD} state, which exhibited the shortest domain separation times, also required the least added bias (maximum bias mode$_{\text{relative}}$ = 0.76). In contrast, the oxi^{metaD} state, which required the highest bias value for domain separation, showed the longest separation times, supporting the idea that greater energy input is needed to achieve large-scale conformational changes in the oxidized state.

In conclusion, the observed increased fluctuations, shorter domain dissociation time, and lower bias potential values in cov models suggest that Cys78–FMN adduct formation and N_5 protonation enable large scale conformational changes of EL222. Red forms displayed mixed features of oxi and cov states, showing reduced fluctuations and intermediate domain separation dynamics.

DNA binding of EL222 in the dark and lit states

Differences in DNA binding between dark and light conditions are supposed to be at the center of transcriptional regulation by EL222 in the cell. Therefore, as a next step, we investigated *in vitro* DNA binding of EL222 in the dark, lit1, and lit2 states by NMR spectroscopy. We chose a nanomolar-affinity double-stranded oligonucleotide of 33 base pairs (DNA33) containing the 12-bp recognition motif previously identified by SELEX methods [7].

DNA binding in the dark

When adding increasing amounts of DNA33 to a $^{13}C/^{15}N$-labeled EL222 sample in the dark, we observed changes in the $^{1}H–^{15}N$ correlation spectra revealing an interaction between DNA33 and EL222 even in the absence of light. The first observation is that a number of amide sites show linear peak shifts with increasing amounts of DNA added (Fig. 5A). This indicates a fast exchange process between free and DNA-bound EL222. In the following, we will refer to this fast exchanging EL222–DNA species as the encounter complex. Similar peak shifts are also observed when using different overall concentrations in equimolar EL222:DNA mixtures (Fig. 5B), as expected for an inter-molecular association. The DNA-binding site of EL222 in this encounter complex can be inferred from the computed $^{1}H/^{15}N$ chemical shift changes upon DNA binding (Supplementary Fig. S15A). Displaying the largest shifts on the crystal structure of EL222 (Supplementary Fig. S15B) revealed that a large part of the HTH domain as well as a helical segment of the LOV domain (Fα) are involved in this transient interaction with DNA. These DNA-induced chemical shift changes correlate with positive surface patches of EL222 (Supplementary Fig. S15C) suggesting that EL222–DNA encounter complex formation is electrostatically-driven. The second observation from these NMR titration data was a loss in peak intensity upon DNA binding for almost all amide sites in EL222 (Supplementary Fig. S15D). An exception is the highly flexible N-terminal

end (Asp19-Asp20-Thr21-Arg22), for which the intensity decreases gradually toward the structured part of the protein, with Asp19 being almost unaffected (Supplementary Fig. S16A). These data can be rationalized by the formation of an EL222–DNA complex that is invisible in the $^{1}H–^{15}N$ spectra, except for the N-terminal residues that remain highly flexible and thus observable by NMR (Supplementary Fig. S16B). The observed intensity loss is not uniform across the structured part of EL222. The signal loss is particularly pronounced in spectral regions affected by encounter complex formation (HTH domain) where, in addition to signal loss due to complex formation, these amide sites are also affected by conformational exchange line broadening due to chemical shift modulation on the micro- to millisecond time scale. The average intensity decrease in the LOV domain provides an estimate of the percentage of EL222 molecules that are involved in complex formation, e.g. $\sim$30% for the 2:1 mixture (indicated by bars in Supplementary Fig. S15D).

The fact that NMR signals of highly flexible sites in the EL222–DNA complex, e.g. N-terminal residues, remain NMR-observable can be exploited to obtain quantitative information on the complex stoichiometry by NMR translational diffusion measurements. We have thus performed ^{1}H amide and ^{1}H methyl DOSY experiments for different EL222:DNA mixtures. While both, amide and methyl-based experiments resulted in similar results, the methyl spectra were of better quality and thus used for further quantification. Two distinct methyl ^{1}H spectral regions (R1 and R2) have been defined for the quantification of translational diffusion properties (Fig. 5C): R1 reports on the population weighted average diffusion properties of free EL222 and the EL222–DNA complex (highly flexible methyl group), while R2 is only sensing the diffusion of monomeric EL222. As expected, the diffusion curves extracted for the R2 region are independent of DNA concentration, while for the R1 region diffusion slows down with increasing amounts of added DNA (Fig. 5D). A quantitative analysis of these data is in agreement with a stoichiometry of two EL222 molecules binding one DNA33 molecule, as expected from literature data [6, 7, 16]. Our NMR data on DNA binding by EL222 in the dark can be summarized by the kinetic scheme shown in Fig. 5E.

DNA binding in the lit states

Finally, we investigated the effect of light on EL222–DNA complex formation by NMR and IR spectroscopies. In order to be able to distinguish the DNA-binding capabilities of the two lit states, we recorded $^{1}H–^{15}N$ correlation spectra of EL222–WT (Fig. 6A) and EL222–C78A (Fig. 6B) in a 2:1 EL222:DNA mixture under continuous low-power blue-light illumination. Under these conditions, the EL222–WT spectra report on lit1 state properties, while the EL222 mutant lacking Cys78 photo-switches directly to lit2, thus providing a convenient way of probing DNA binding in the lit2 state. In both cases, the NMR signal intensity (except for the N-terminal tail) is further reduced, indicative of a shift in the population equilibrium toward the EL222–DNA complex. Interestingly, 100% complex formation is only observed for the lit1 state. In the lit2 state, $\sim$25% of the EL222 molecules remain in an exchange between monomeric EL222 and the encounter complex. The IR double difference spectra of EL222:DNA 2:1 mixtures suggest DNA-dependent conformational changes in secondary structure (amide I' band reporter) and oligomerization (pCNF reporter), which probably arise from the
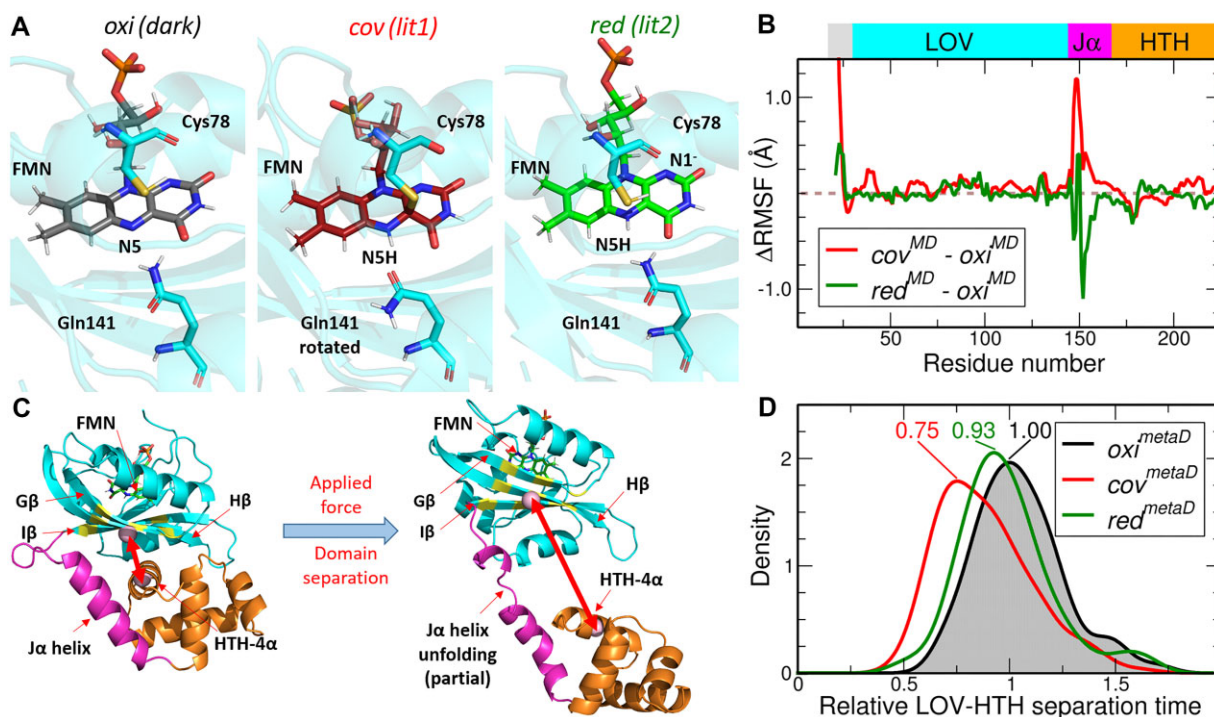
Figure 4. Molecular modelings suggest differential dynamics and "opening" propensities of the three EL222 states. (**A**) Molecular models of oxidized (*oxi*) FMN (dark), covalently bound (*cov*) FMN (lit1), and fully reduced (*red*) FMN (lit2) used for MD simulations, highlighting chemical differences in the FMN-binding pocket of EL222 due to (de)protonation, adduct formation, and glutamine rotation. Relevant amino acids in the LOV-binding site (Cys78 and Gln141) are depicted as sticks. (**B**) Differential root mean square fluctuation (ΔRMSF) plot of Cα atoms from 3 μs cumulative MD simulations of cov^{MD} and red^{MD} relative to oxi^{MD}. (**C**) Representation of LOV–HTH domain separation in EL222 employing metadynamics (metaD) with a bias potential applied along an inter-domain distance defined as the distance between the center-of-mass of HTH-4α residues and the center-of-mass of selected residues in Iβ, Hβ, and Gβ regions. The linker sequences, including the Iβ-Jα loop and the Jα-helix, and the FMN chromophore are also shown. (**D**) Density plots of relative LOV–HTH separation time (normalized to oxidized state mode value) extracted from metaD simulations (160 replicas by 50 ns). Normalized relative domain separation times in oxi^{metaD}, cov^{metaD}, and red^{metaD} are indicated for each distribution.

NMR-invisible species (Fig. 6C). In other words, free and DNA-bound EL222 dimers are structurally different.

Although the lit1 and lit2 spectra are qualitatively similar, the observed amplitude and frequency shifts indicate DNA-dependent structural differences between the two lit states. Overall, we can extract two novel conclusions: (i) covalent bond formation is not essential for DNA binding but its presence increases the probability of the interaction between EL222 and DNA, and (ii) FMN reduction is also not essential for DNA binding but necessary to shift the equilibrium toward long-lived EL222:DNA (2:1) complexes (Fig. 6D). Therefore, EL222 domain separation, dimerization, and DNA binding are coupled processes that can be influenced by light, which changes the free energy of individual states, thus shifting the population equilibria as illustrated in Fig. 7.

Discussion

By employing a combination of complementary methods in solution (NMR, IR, and UV–visible spectroscopy), *in silico* (MD and metaD simulations), and *in crystallo* (MX), our study provides novel insights into the structural and dynamical changes that EL222 undergoes during its photocycle. The different redox/adduct states of FMN (*oxi*, *cov*, and *red*) give rise to three EL222 states (dark, lit1, and lit2) that show distinct behaviors with respect to their conformational dynamics (domain opening), oligomerization propensity, and DNA-binding ability.

Our lit1 state corresponds to the previously described states of LOV proteins obtained after continuous illumination for short times, referred to as lit [6, 52], light [53], signaling [54], A390 [55], or adduct [56] state. The distinctive feature of lit1 is the presence of a covalent bond between FMN and the active-site cysteine which is breakable in the dark. In addition, we could structurally and dynamically characterize a new photo-induced state of EL222 bearing fully reduced FMN, named lit2 which, to the best of our knowledge, has not been described before. However, LOV domains containing fully reduced FMN have been previously detected by UV–visible spectroscopy after prolonged photoexcitation [37] or upon chemical reduction with sodium dithionite [38]. Lit2 has mixed features of dark and lit1 states. On the one hand, dark and lit2 states have no covalent bond between FMN and Cys78. On the other hand, both lit1 and lit2 share an enhanced oligomerization propensity and the ability to form 2:1 complexes with DNA. One significant difference between lit1 and lit2 is that only lit1 can form 100% EL222:DNA complexes after mixing 2 moles of EL222 with 1 mole of DNA. Adduct scission in the lit2 state is compatible with the metastability and reversibility of the C-S bond [57].

The solution lit2 state of EL222 may have been previously undetected due to different irradiation conditions. Here we were applying continuous illumination in an airtight Shigemi tube, while pulsed illumination in a standard 5 mm NMR tube was used in previous work [6]. The combination of prolonged illumination and minimal oxygen exchange are key for the
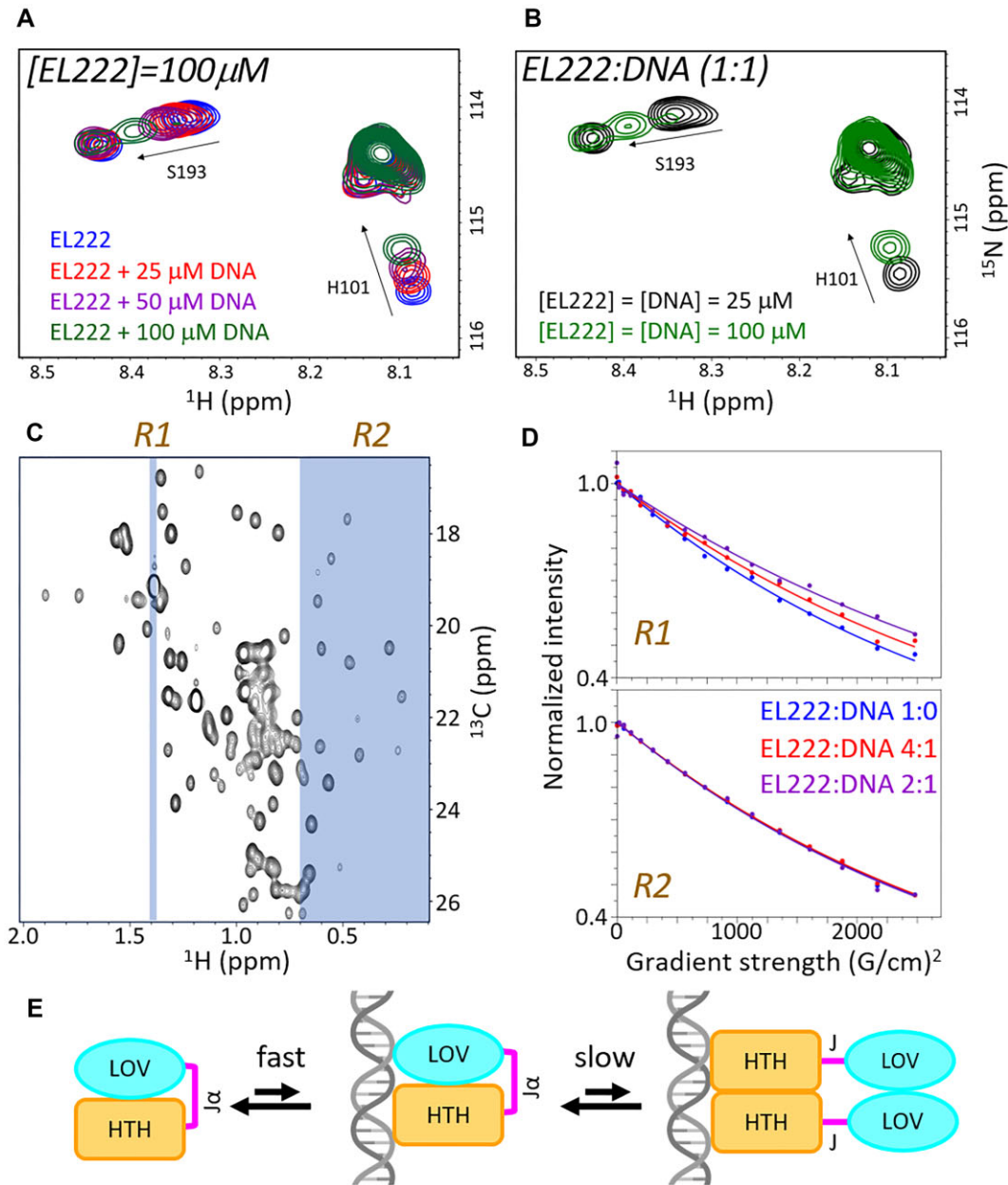
Figure 5. EL222 interacts with DNA in the absence of light. (**A**) ^{1}H–^{15}N NMR spectral region of EL222: DNA mixtures highlighting two residues that show linear chemical shift changes with increasing DNA concentration. (**B**) The same ^{1}H–^{15}N NMR spectral region highlighting the effect of total concentration of equimolar EL222–C78A mixtures on the NMR chemical shifts. (**C**) Methyl region of ^{1}H–^{13}C spectra of EL222. The two highlighted ^{1}H spectral regions correspond to a highly flexible methyl group in the monomer and complex (R1), and a number of well-structured methyl groups located in the hydrophobic protein core (R2). (**D**) 1D methyl ^{1}H DOSY NMR data. The NMR intensity, integrated over the spectral region (R1 or R2) is plotted as a function of gradient strength. (**E**) Model of EL222–DNA interactions in the dark. Monomeric EL222 is in fast exchange between DNA-free and DNA-bound (monomeric encounter complex) forms. This encounter complex is in slow exchange with EL222–DNA complexes of 2:1 stoichiometry.

photoconversion from lit1 to lit2 states. Because of the requirement of high irradiances and anaerobic conditions, we do not believe that the lit2 state can be readily formed from "canonical" LOV photosensors, i.e. those containing the reactive cysteine, under common environmental conditions. However, LOV photoreceptors carrying alternative residues at that position, e.g. histidine, have been described [42]. Thus, the lit2 state may be the prevalent species in these "noncanonical" LOV proteins upon blue light absorption.

We cannot exclude that the lit2 state is also impacted by oxidative damage due to prolonged light exposure [58, 59],

potentially leading to protein aggregation [60]. Indeed, flavin-binding fluorescent proteins derived from the LOV domain have been engineered as genetically encoded photosensitizers that generate toxic reactive oxygen species (ROS) [61]. We have evidence for the oxidative modification of certain amino acids in EL222, in particular the 2-oxo-histidine residue found in the crystal structures. Such a modification was previously observed in structurally similar proteins such as miniSOG (PDB ID: 6GPV), a flavin-containing protein developed from the LOV2 domain of *Arabidopsis thaliana* phototropin 2 specifically to produce singlet oxygen upon illumination [62].
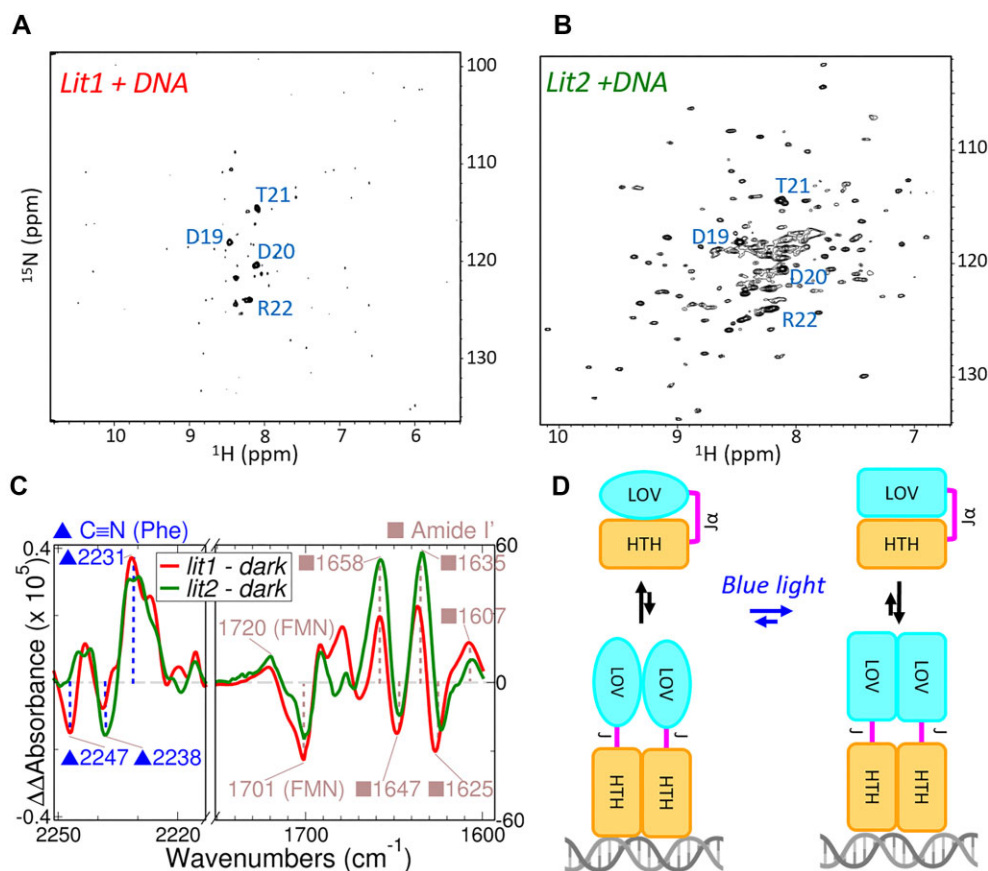
Figure 6. The two lit states interact with DNA with distinct efficiencies and lifetimes. ^{1}H–^{15}N correlation spectra of 2:1 EL222:DNA mixtures of (**A**) EL222–WT (100 μM) and (**B**) EL222–C78A (100 μM) recorded under weak blue-light illumination. The flexible N-terminal residues that remain visible upon complex formation are annotated. (**C**) Double difference species-associated infrared spectra of EL222–W31pCNF in the nitrile (C≡N) stretching region (left) and EL222-WT in the amide I' (C=O) region (right) calculated as the difference between the light-minus-dark spectra in the presence minus the absence of DNA. (**D**) Model of EL222–DNA interactions upon blue-light illumination. Light shifts the binding equilibrium toward DNA-bound EL222 dimers. Elliptical and rectangular shapes denote the slightly different conformation of the LOV domain arising from changes in the redox/protonation state of FMN and presence/absence of a covalent bond; pCNF, *para*-cyano-L-phenylalanine.

The increase in ROS production has been associated to the release of FMN to the solvent [58], which we do not observe in our experiments. Thus, although oxidized residues may be found in the lit2 state, it is unlikely that they become the dominant factor responsible for the conformational changes. Instead, we argue that the main driving force underlying the formation of the lit2 state is the loss of the FMN–Cys covalent bonding and full reduction of the embedded FMN chromophore. Massive LOV aggregation, i.e. clustering, has only been reported for two LOV proteins under certain conditions [60, 63]. Most LOV domains undergo reversible oligomerization up to tetramers. For instance, RsLOV undergoes light-induced dimer-to-monomer transitions [64], while in AtLOV1 dark-state dimers assemble into lit-state tetramers [65]. Similar to EL222, light-induced dimerization is also part of the activation mechanism of VIVID [66] and aureochrome-1 [67]. In line with the latter studies, we also found that EL222 undergoes reversible oligomerization from both lit1 and lit2 states, although the exact stoichiometry remains unknown.

The slow kinetics of lit1-to-lit2 photoconversion in EL222–WT (time scale of hours) contrasts with the fast formation of lit2 in EL222–C78A (less than one minute), and with the ultrafast primary flavin photoreactions (sub-second time scale). Sub-millisecond LOV domain photochemistry is essentially the same for all LOV variants with only minor differences in the rate constants [20, 55, 68, 69]. Absorption of blue light (∼400–480 nm) by the embedded FMN triggers the formation of the singlet excited state almost instantaneously. The singlet decays to the triplet state in ∼2–4 ns via intersystem crossing. Finally, the triplet decays into the adduct state on time-scales of 0.2–10 μs. The slow accumulation of lit2 in LOV versions carrying the reactive cysteine is compatible with a short-lived triplet state and the low quantum yield of FMN reduction to hydroquinone [70]. On the other hand, the rapid formation of lit2 state in EL222-C78A suggests that it originates from the long-lived triplet state (∼1 ms) [20], most likely preceded by a short-lived neutral semiquinone (NSQ) state. Interestingly, the isolated LOV domain of EL222 converts to the lit2 state much faster than the two-domain EL222 protein. This result suggests that the HTH domain stabilizes somehow the lit1 state relative to lit2.

Accumulated evidence suggests that the reduction and protonation state of FMN, rather than the presence of a covalent bond between FMN and the LOV core, is the main determinant for all subsequent conformational changes [42, 54]. Flavoproteins in general are sensitive to the redox state of their bound flavin [71, 72], and LOV proteins in particular may play a role in redox sensing in the cell [73, 74]. The main
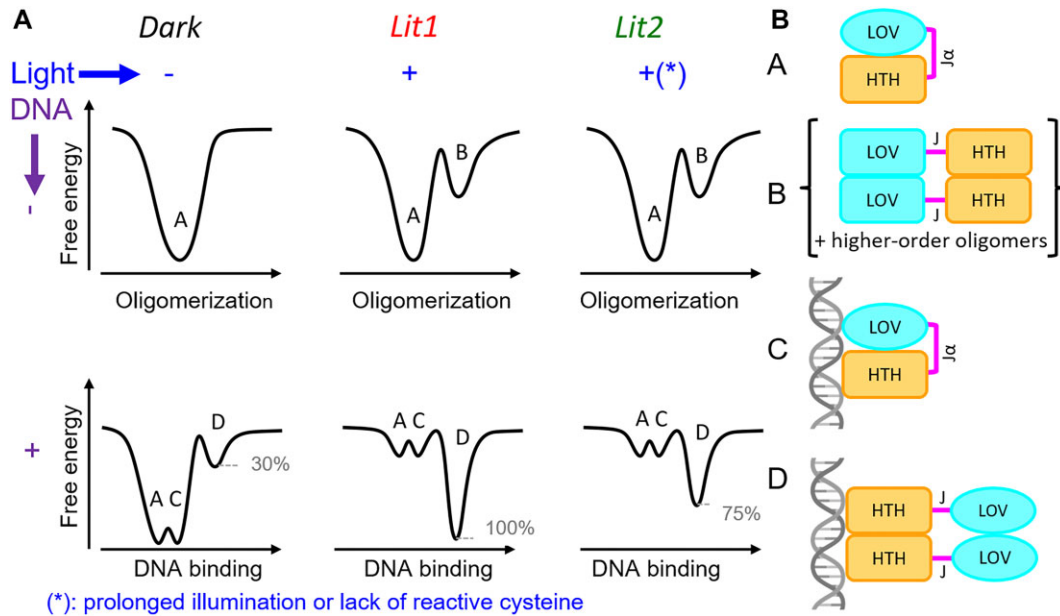
Figure 7. EL222 free-energy landscape model of photoinduced oligomerization and DNA binding. (**A**) In the absence of DNA, the dark state is characterized by a nearly 100% monomeric conformation (A), while the lit1 and lit2 states feature a mixture of monomeric (A) and oligomeric (B) species. In the dark, EL222 transiently binds to DNA as monomer (C species), and also forms a small amount of 2:1 EL222:DNA complex (D species). In presence of blue light, EL222 oligomerization and DNA binding is significantly enhanced with the largest population shift observed for lit1. (**B**) Proposed structural models of A (free monomer), B (free oligomer), C (DNA-bound monomer), and D (DNA-bound oligomer) species. Note that the exact conformation of A, B, C, and D species will be slightly different in the dark, lit1, and lit2 states.

structural changes in LOV proteins occur concomitantly with adduct formation [55, 69, 75]. Such changes depend on the modules accompanying the LOV domain. For instance, large-scale structural changes do not occur during activation of the blue-light receptor YtvA [76], while unfolding of the helices flanking the core LOV domain, A'α at the N-terminus and Jα at the C-terminus, has been reported for aureochromes [77, 78] and truncated versions of *Avena sativa* phototropin 1 [79–81]. Photoinduced unfolding of α-helices has been observed for EL222 but so far has not been unambiguously assigned to a particular region [15]. Contrary to FMN, which is essential for signaling, conserved residues in the LOV domain are not critical unless they affect FMN binding. Cysteine-less LOV variants can still transduce signals, albeit with lower efficiency and significant production of potentially damaging ROS [42, 82]. A conserved glutamine residue appears to sense the protonation state at N_5 via rotation of its side-chain, a movement that provokes long-range changes in the LOV domain [52, 69, 80, 83]. However, glutamine-less variants can still be physiologically active when illuminated, suggesting that the coupling between FMN photochemistry and LOV holoprotein activation is more complex than previously predicted and likely proceeds via multiple pathways [84]. Our results lend support to the view that the dynamic behavior of EL222 changes significantly after illumination and this shifts the conformational (domain separation, secondary structure) and oligomerization equilibria.

Transcription factors can bind DNA cooperatively thereby strengthening their affinity [85, 86]. Here we show that the DNA-binding activity of EL222 is not an infinitely cooperative process, with no DNA interaction in the dark and complete association under light conditions. Rather, the different redox/adduct states of FMN in the dark, lit1, and lit2 states, differ in their dimerization (or more generally, oligomeriza-

tion) properties, likely because of an altered propensity to populate an "open" conformation. Specifically, the lit1 state has the highest structural plasticity, i.e. tendency to change the secondary structure and oligomerize, and this may explain the increased DNA-binding ability. In the presence of DNA, an EL222–DNA heterocomplex, predominantly of 1:1 stoichiometry, can be assembled, even in the dark. The complex assembly and disassembly kinetics, however, critically depend on the redox state of the embedded FMN chromophore, and thus on light. A stable 2:1 (protein:DNA) complex formation is most efficient in the lit1 state that is characterized by N_5-protonated FMN and cysteinyl adduct formation. At this point, we can only speculate about the transcriptional activity of the different states. We expect that the encounter complex seen in the dark will have little ability to activate gene expression but may be important to determine the basal levels of transcription. Regarding the lit2 state, we hypothesize that it could probably sustain gene transcription, although less efficiently than the lit1 state. Since increasing the intensity of light is one way to achieve higher transcriptional output from optogenetic systems [8–10, 63], our findings may be taken into account to design more efficient EL222-inducible systems with improved dynamic ranges.

Our results highlight the complementarity between different structural and biophysical methods. MX delivers near-atomic-resolution structural information in the crystalline state but it is unclear to what extent restrictions imposed by crystal packing are affecting EL222 conformational changes [87]. NMR is ideally suited to identify conformational subpopulations and their exchange kinetics in solution [88]. It also provides atomic resolution structural and dynamical information, as long as the particle sizes are small enough. IR spectroscopy is sensitive to protein secondary structure changes and oligomerization, also in solution, but without any

size limitation. However, IR data are difficult to interpret in the absence of additional information [47]. UV–visible spectroscopy is an excellent choice to monitor structural and electronic changes in FMN, including the formation of an FMN–cysteine adduct but provides virtually no information beyond the chromophore. Therefore, only the combination of these different techniques allowed us to derive a comprehensive picture of the EL222 photocycle in the absence and presence of DNA.

Acknowledgements

Supplementary data

Supplementary data is available at NAR online.

Conflict of interest

None declared.

Funding

Data availability

X-ray structures have been deposited in the Protein Data Bank under accession codes 8A5R (EL222 dark) and 8A5S (mix of EL222 dark and EL222 lit1). NMR chemical shifts have been deposited in the Biological Magnetic Resonance Data Bank under accession codes BMRB 52621 (EL222 dark), BMRB 52620 (EL222 lit1), and BMRB 52622 (EL222 lit2). All input files required for classical MD and metaD simulations for the *oxi*, *cov*, and *red* models in GROMACS, including configuration files, COLVAR and HILLS files, and postprocessing scripts, are provided in Zenodo repository, accessible at https://doi.org/10.5281/zenodo.13889603. All infrared and UV–visible spectra can be found in the same Zenodo link.

References

1. Briggs WR. The LOV domain: a chromophore module servicing multiple photoreceptors. *J Biomed Sci* 2007;**14**:499–504. https://doi.org/10.1007/s11373-007-9162-6
2. Demarsy E, Fankhauser C. Higher plants use LOV to perceive blue light. *Curr Opin Plant Biol* 2009;**12**:69–74. https://doi.org/10.1016/j.pbi.2008.09.002
3. Herrou J, Crosson S. Function, structure and mechanism of bacterial photosensory LOV proteins. *Nat Rev Micro* 2011;**9**:713–23. https://doi.org/10.1038/nrmicro2622
4. Losi A, Gärtner W. Solving blue light riddles: new lessons from flavin-binding LOV photoreceptors. *Photochem Photobiol* 2017;**93**:141–58. https://doi.org/10.1111/php.12674
5. Flores-Ibarra A, Maia RNA, Olasz B *et al.* Light-oxygen-voltage (LOV)-sensing domains: activation mechanism and optogenetic stimulation. *J Mol Biol* 2024;**436**:168356. https://doi.org/10.1016/j.jmb.2023.168356
6. Nash AI, McNulty R, Shillito ME *et al.* Structural basis of photosensitivity in a bacterial light-oxygen-voltage/helix-turn-helix (LOV-HTH) DNA-binding protein. *Proc Natl Acad Sci* 2011;**108**:9449–54. https://doi.org/10.1073/pnas.1100262108
7. Rivera-Cancel G, Motta-Mena LB, Gardner KH. Identification of natural and artificial DNA substrates for light-activated LOV-HTH transcription factor EL222. *Biochemistry* 2012;**51**:10024–34. https://doi.org/10.1021/bi301306t
8. Motta-Mena LB, Reade A, Mallory MJ *et al.* An optogenetic gene expression system with rapid activation and deactivation kinetics. *Nat Chem Biol* 2014;**10**:196–202. https://doi.org/10.1038/nchembio.1430
9. Reade A, Motta-Mena LB, Gardner KH *et al.* TAEL: a zebrafish-optimized optogenetic gene expression system with fine spatial and temporal control. *Development* 2016;**144**:345–55. https://doi.org/10.1242/dev.139238
10. Wang Z, Yan Y, Zhang H. Design and characterization of an optogenetic system in Pichia pastoris. *ACS Synth Biol* 2022;**11**:297–307. https://doi.org/10.1021/acssynbio.1c00422

11. Ochoa-Fernandez R, Abel NB, Wieland F-G *et al.* Optogenetic control of gene expression in plants in the presence of ambient white light. *Nat Methods* 2020;**17**:717–25. https://doi.org/10.1038/s41592-020-0868-y

12. Jayaraman P, Devarajan K, Chua TK *et al.* Blue light-mediated transcriptional activation and repression of gene expression in bacteria. *Nucleic Acids Res* 2016;**44**:6994–7005. https://doi.org/10.1093/nar/gkw548

13. Gligorovski V, Sadeghi A, Rahi SJ. Multidimensional characterization of inducible promoters and a highly light-sensitive LOV-transcription factor. *Nat Commun* 2023;**14**:3810. https://doi.org/10.1038/s41467-023-38959-8

14. Cleere MM, Gardner KH. Optogenetic control of phosphate-responsive genes using single component fusion proteins in Saccharomyces cerevisiae. *ACS Synth Biol* 2024; **13**:4085–98. https://doi.org/10.1021/acssynbio.4c00529

15. Chaudhari AS, Chatterjee A, Domingos CAO *et al.* Genetically encoded non-canonical amino acids reveal asynchronous dark reversion of chromophore, backbone, and side-chains in EL222. *Protein Sci* 2023;**32**:e4590. https://doi.org/10.1002/pro.4590

16. Takakado A, Nakasone Y, Terazima M. Sequential DNA binding and dimerization processes of the photosensory protein EL222. *Biochemistry* 2018;**57**:1603–10. https://doi.org/10.1021/acs.biochem.7b01206

17. Takakado A, Nakasone Y, Terazima M. Photoinduced dimerization of a photosensory DNA-binding protein EL222 and its LOV domain. *Phys Chem Chem Phys* 2017;**19**:24855–65. https://doi.org/10.1039/C7CP03686H

18. Zoltowski BD, Motta-Mena LB, Gardner KH. Blue light-induced dimerization of a bacterial LOV–HTH DNA-binding protein. *Biochemistry* 2013;**52**:6653–61. https://doi.org/10.1021/bi401040m

19. Zoltowski BD, Nash AI, Gardner KH. Variations in protein–Flavin hydrogen bonding in a light, oxygen, voltage domain produce non-arrhenius kinetics of adduct decay. *Biochemistry* 2011;**50**:8771–9. https://doi.org/10.1021/bi200976a

20. Liu Y, Chaudhari AS, Chatterjee A *et al.* Sub-millisecond photoinduced dynamics of free and EL222-bound FMN by stimulated raman and visible absorption spectroscopies. *Biomolecules* 2023;**13**:161. https://doi.org/10.3390/biom13010161

21. Favier A, Brutscher B. Recovering lost magnetization: polarization enhancement in biomolecular NMR. *J Biomol NMR* 2011;**49**:9–15. https://doi.org/10.1007/s10858-010-9461-5

22. Favier A, Brutscher B. NMRlib: user-friendly pulse sequence tools for Bruker NMR spectrometers. *J Biomol NMR* 2019;**73**:199–211. https://doi.org/10.1007/s10858-019-00249-1

23. Johnson CS. Diffusion ordered nuclear magnetic resonance spectroscopy: principles and applications. *Prog Nucl Magn Reson Spectrosc* 1999;**34**:203–56. https://doi.org/10.1016/S0079-6565(99)00003-5

24. Farrow NA, Muhandiram R, Singer AU *et al.* Backbone dynamics of a free and a phosphopeptide-complexed src homology 2 domain studied by 15N NMR relaxation. *Biochemistry* 1994;**33**:5984–6003. https://doi.org/10.1021/bi00185a040

25. Lee D, Hilty C, Wider G *et al.* Effective rotational correlation times of proteins from NMR relaxation interference. *J Magn Reson* 2006;**178**:72–6. https://doi.org/10.1016/j.jmr.2005.08.014

26. Christou N-E, Ayala I, Giandoreggio-Barranco K *et al.* NMR reveals light-induced changes in the dynamics of a photoswitchable fluorescent protein. *Biophys J* 2019;**117**:2087–100. https://doi.org/10.1016/j.bpj.2019.10.035

27. Wang J, Cieplak P, Kollman PA. How well does a restrained electrostatic potential (RESP) model perform in calculating conformational energies of organic and biological molecules? *J Comput Chem* 2000;**21**:1049–74. https://doi.org/10.1002/1096-987X(200009)21:12%3c1049:: AID-JCC3%3e3.0.CO;2-F

28. Bayly CI, Cieplak P, Cornell W *et al.* A well-behaved electrostatic potential based method using charge restraints for deriving atomic charges: the RESP model. *J Phys Chem* 1993;**97**:10269–80. https://doi.org/10.1021/j100142a004

29. Darden T, York D, Pedersen L. Particle mesh Ewald: an N·log(N) method for Ewald sums in large systems. *J Chem Phys* 1993;**98**:10089–92. https://doi.org/10.1063/1.464397

30. Essmann U, Perera L, Berkowitz ML *et al.* A smooth particle mesh Ewald method. *J Chem Phys* 1995;**103**:8577–93. https://doi.org/10.1063/1.470117

31. Van Der Spoel D, Lindahl E, Hess B *et al.* GROMACS: fast, flexible, and free. *J Comput Chem* 2005;**26**:1701–18. https://doi.org/10.1002/jcc.20291

32. Abraham MJ, Murtola T, Schulz R *et al.* GROMACS: high performance molecular simulations through multi-level parallelism from laptops to supercomputers. *SoftwareX* 2015;**1-2**:19–25. https://doi.org/10.1016/j.softx.2015.06.001

33. Tribello GA, Bonomi M, Branduardi D *et al.* PLUMED 2: new feathers for an old bird. *Comput Phys Commun* 2014;**185**:604–13. https://doi.org/10.1016/j.cpc.2013.09.018

34. PLUMED Consortium Promoting transparency and reproducibility in enhanced molecular simulations. *Nat Methods* 2019;**16**:670–3. https://doi.org/10.1038/s41592-019-0506-8

35. Muller F, Müller F. *Chemistry and Biochemistry of Flavoenzymes*. Boca Raton, FL, USA: CRC Press, 2018.

36. Moonen CTW, Vervoort J, Mueller F. Reinvestigation of the structure of oxidized and reduced flavin: carbon-13 and nitrogen-15 nuclear magnetic resonance study. *Biochemistry* 1984;**23**:4859–67. https://doi.org/10.1021/bi00316a007

37. Salomon M, Eisenreich W, Dürr H *et al.* 2001; An optomechanical transducer in the blue light receptor phototropin from *Avena sativa*. *Proc Natl Acad Sci*, **98**:12357–61. https://doi.org/10.1073/pnas.221455298

38. Eisenreich W, Kemter K, Bacher A *et al.* 13C-, 15N- and 31P-NMR studies of oxidized and reduced low molecular mass thioredoxin reductase and some mutant proteins. *Eur J Biochem* 2004;**271**:1437–52. https://doi.org/10.1111/j.1432-1033.2004.04043.x

39. Barth A. The infrared absorption of amino acid side chains. *Prog Biophys Mol Biol* 2000;**74**:141–73. https://doi.org/10.1016/S0079-6107(00)00021-3

40. Deniz E, Schmidt-Engler JM, Ulrich K *et al.* SH—It happens: S–H bonds as intrinsic 2D-IR labels in proteins. *J Chem Phys* 2022;**157**: 135102. https://doi.org/10.1063/5.0107057

41. Hemmer S, Siedhoff NE, Werner S *et al.* Machine learning-assisted engineering of light, oxygen, voltage photoreceptor adduct lifetime. *JACS Au* 2023;**3**:3311–23. https://doi.org/10.1021/jacsau.3c00440

42. Yee EF, Diensthuber RP, Vaidya AT *et al.* Signal transduction in light–oxygen–voltage receptors lacking the adduct-forming cysteine residue. *Nat Commun* 2015;**6**:10079. https://doi.org/10.1038/ncomms10079

43. Spera S, Bax A. Empirical correlation between protein backbone conformation and C.alpha. And C.beta. 13C nuclear magnetic resonance chemical shifts. *J Am Chem Soc* 1991;**113**:5490–2. https://doi.org/10.1021/ja00014a071

44. Eliezer D, Yao J, Dyson HJ *et al.* Structural and dynamic characterization of partially folded states of apomyoglobin and implications for protein folding. *Nat Struct Mol Biol* 1998;**18**:148–55. https://doi.org/10.1038/nsb0298-148

45. Shen Y, Delaglio F, Cornilescu G *et al.* TALOS+: a hybrid method for predicting protein backbone torsion angles from NMR chemical shifts. *J Biomol NMR* 2009;**44**:213–23. https://doi.org/10.1007/s10858-009-9333-z

46. Cornilescu G, Delaglio F, Bax A. Protein backbone angle restraints from searching a database for chemical shift and sequence homology. *J Biomol NMR* 1999;**13**:289–302. https://doi.org/10.1023/A:1008392405740

47. Lorenz-Fonfria VA. Infrared difference spectroscopy of proteins: from bands to bonds. *Chem Rev* 2020;**120**:3466–576. https://doi.org/10.1021/acs.chemrev.9b00449

48. Chaudhari AS, Semanat EC, Martel A *et al*. Light-induced oligomerization of the transcription factor EL222. *Acta Crystallogr A Found Adv* 2021;**77**:C868. https://doi.org/10.1107/S0108767321088309

49. Xiao S, Ibrahim MT, Verkhivker GM *et al*. β-sheets mediate the conformational change and allosteric signal transmission between the AsLOV2 termini. *J Comput Chem* 2024; **45**:1493–1504. https://doi.org/10.1002/jcc.27344

50. Bonomi M, Branduardi D, Bussi G *et al*. PLUMED: a portable plugin for free-energy calculations with molecular dynamics. *Comput Phys Commun* 2009;**180**:1961–72. https://doi.org/10.1016/j.cpc.2009.05.011

51. Bernardi RC, Melo MCR, Schulten K. Enhanced sampling techniques in molecular dynamics simulations of biological systems. *Biochim Biophys Gen Sub* 2015;**1850**:872–7. https://doi.org/10.1016/j.bbagen.2014.10.019

52. Nash AI, Ko W-H, Harper SM *et al*. A conserved glutamine plays a Central role in LOV domain signal transmission and its duration. *Biochemistry* 2008;**47**:13842–9. https://doi.org/10.1021/bi801430e

53. Pudasaini A, Green R, Song YH *et al*. Steric and electronic interactions at Gln154 in ZEITLUPE induce reorganization of the LOV domain dimer interface. *Biochemistry* 2021;**60**:95–103. https://doi.org/10.1021/acs.biochem.0c00819

54. García de Fuentes A, Möglich A. Reduction midpoint potential of a paradigm light–oxygen–voltage receptor and its modulation by methionine residues. *RSC Chem Biol* 2024;**4**:530–43. https://doi.org/10.1039/D4CB00056K

55. Iuliano JN, Gil AA, Laptenok SP *et al*. Variation in LOV photoreceptor activation dynamics probed by time-resolved infrared spectroscopy. *Biochemistry* 2018;**57**:620–30. https://doi.org/10.1021/acs.biochem.7b01040

56. Arinkin V, Granzin J, Krauss U *et al*. Structural determinants underlying the adduct lifetime in the LOV proteins of *Pseudomonas putida*. *FEBS J* 2021;**288**:4955–72. https://doi.org/10.1111/febs.15785

57. Kennis JTM, van Stokkum IHM, Crosson S *et al*. The LOV2 domain of phototropin: a reversible photochromic switch. *J Am Chem Soc* 2004;**126**:4512–3. https://doi.org/10.1021/ja031840r

58. Petrenčáková M, Filandr F, Hovan A *et al*. Photoinduced damage of AsLOV2 domain is accompanied by increased singlet oxygen production due to flavin dissociation. *Sci Rep* 2020;**10**:4119. https://doi.org/10.1038/s41598-020-60861-2

59. Gasset M, Hernández-Candia CN, Casas-Flores S *et al*. Light induces oxidative damage and protein stability in the fungal photoreceptor Vivid. *PLoS One* 2018;**13**:e0201028. https://doi.org/10.1371/journal.pone.0201028

60. Gutiérrez-Medina B, Hernández-Candia CN. Aggregation kinetics of the protein photoreceptor vivid. *Biochim Biophys Acta* 2021;**1869**:140620. https://doi.org/10.1016/j.bbapap.2021.140620

61. Endres S, Wingen M, Torra J *et al*. An optogenetic toolbox of LOV-based photosensitizers for light-driven killing of bacteria. *Sci Rep* 2018;**8**:15021. https://doi.org/10.1038/s41598-018-33291-4

62. Torra J, Lafaye C, Signor L *et al*. Tailing miniSOG: structural bases of the complex photophysics of a flavin-binding singlet oxygen photosensitizing protein. *Sci Rep* 2019;**9**:2428. https://doi.org/10.1038/s41598-019-38955-3

63. Pal AA, Benman W, Mumford TR *et al*. Optogenetic clustering and membrane translocation of the BcLOV4 photoreceptor. *Proc Natl Acad Sci USA* 2023;**120**:e2221615120. https://doi.org/10.1073/pnas.2221615120

64. Conrad KS, Bilwes AM, Crane BR. Light-induced subunit dissociation by a light–oxygen–voltage domain photoreceptor from *Rhodobacter sphaeroides*. *Biochemistry* 2013;**52**:378–91. https://doi.org/10.1021/bi3015373

65. Nakasone Y, Zikihara K, Tokutomi S *et al*. Photochemistry of arabidopsis phototropin 1 LOV1: transient tetramerization. *Photochem Photobiol Sci* 2013;**12**:1171–9. https://doi.org/10.1039/C3PP50047K

66. Vaidya AT, Chen C-H, Dunlap JC *et al*. Structure of a light-activated LOV protein dimer that regulates transcription. *Sci Signal* 2011;**4**:ra50. https://doi.org/10.1126/scisignal.2001945

67. Hisatomi O, Nakatani Y, Takeuchi K *et al*. Blue light-induced dimerization of monomeric aureochrome-1 enhances its affinity for the target sequence. *J Biol Chem* 2014;**289**:17379–91. https://doi.org/10.1074/jbc.M114.554618

68. Conrad KS, Manahan CC, Crane BR. Photochemistry of flavoprotein light sensors. *Nat Chem Biol* 2014;**10**:801–9. https://doi.org/10.1038/nchembio.1633

69. Andrikopoulos PC, Chaudhari AS, Liu Y *et al*. QM calculations predict the energetics and infrared spectra of transient glutamine isomers in LOV photoreceptors. *Phys Chem Chem Phys* 2021;**23**:13934–50. https://doi.org/10.1039/D1CP00447F

70. Song SH, Dick B, Penzkofer A *et al*. Photo-reduction of flavin mononucleotide to semiquinone form in LOV domain mutants of blue-light receptor phot from Chlamydomonas reinhardtii. *J Photochem Photobiol, B* 2007;**87**:37–48. https://doi.org/10.1016/j.jphotobiol.2006.12.007

71. Becker DF, Zhu W, Moxley MA. Flavin redox switching of protein functions. *Antioxid Redox Signal* 2011;**14**:1079–91. https://doi.org/10.1089/ars.2010.3417

72. Senda T, Senda M, Kimura S *et al*. Redox control of protein conformation in flavoproteins. *Antioxid Redox Signal* 2009;**11**:1741–66. https://doi.org/10.1089/ars.2008.2348

73. Purcell EB, McDonald CA, Palfey BA *et al*. An analysis of the solution structure and signaling mechanism of LovK, a sensor histidine kinase integrating light and redox signals. *Biochemistry* 2010;**49**:6761–70. https://doi.org/10.1021/bi1006404

74. Bury A, Hellingwerf KJ. On the In Vivo Redox State of Flavin-Containing Photosensory Receptor Proteins. In: Weber S, Schleicher E (eds.), *Flavins and FlavoproteinsMethods in Molecular Biology*. Vol. **1146**. New York, NY: Humana Press. 2014, 177–90. https://doi.org/10.1007/978-1-4939-0452-5_9

75. Eitoku T, Nakasone Y, Zikihara K *et al*. Photochemical intermediates of arabidopsis phototropin 2 LOV domains associated with conformational changes. *J Mol Biol* 2007;**371**:1290–303. https://doi.org/10.1016/j.jmb.2007.06.035

76. Jurk M, Dorn M, Kikhney A *et al*. The switch that does not flip: the blue-light receptor YtvA from *Bacillus subtilis* adopts an elongated dimer conformation independent of the activation State as revealed by a combined AUC and SAXS study. *J Mol Biol* 2010;**403**:78–87. https://doi.org/10.1016/j.jmb.2010.08.036

77. Herman E, Kottke T. Allosterically regulated unfolding of the A′α helix exposes the dimerization site of the blue-light-sensing aureochrome-LOV domain. *Biochemistry* 2015;**54**:1484–92. https://doi.org/10.1021/bi501509z

78. Herman E, Sachse M, Kroth PG *et al*. Blue-light-induced unfolding of the Jα helix allows for the dimerization of aureochrome-LOV from the Diatom phaeodactylum tricornutum. *Biochemistry* 2013;**52**:3094–101. https://doi.org/10.1021/bi400197u

79. Konold PE, Mathes T, Weißenborn J *et al*. Unfolding of the C-terminal jα helix in the LOV2 photoreceptor domain observed by time-resolved vibrational spectroscopy. *J Phys Chem Lett* 2016;**7**:3472–6. https://doi.org/10.1021/acs.jpclett.6b01484

80. Iuliano JN, Collado JT, Gil AA *et al*. Unraveling the mechanism of a LOV domain optogenetic sensor: a glutamine lever induces unfolding of the Jα helix. *ACS Chem Biol* 2020;**15**:2752–65. https://doi.org/10.1021/acschembio.0c00543

81. Kim C, Yun SR, Lee SJ *et al*. Structural dynamics of protein-protein association involved in the light-induced transition of Avena sativa LOV2 protein. *Nat Commun* 2024;**15**:6991. https://doi.org/10.1038/s41467-024-51461-z

82. Kopka B, Magerl K, Savitsky A *et al*. Electron transfer pathways in a light, oxygen, voltage (LOV) protein devoid of the photoactive

cysteine. *Sci Rep* 2017;**7**:13346.
https://doi.org/10.1038/s41598-017-13420-1

83. Ganguly A, Thiel W, Crane BR. Glutamine amide flip elicits long distance allosteric responses in the LOV protein vivid. *J Am Chem Soc* 2017;**139**:2972–80. https://doi.org/10.1021/jacs.6b10701

84. Dietler J, Gelfert R, Kaiser J *et al*. Signal transduction in light-oxygen-voltage receptors lacking the active-site glutamine. *Nat Commun* 2022;**13**:2618.
https://doi.org/10.1038/s41467-022-30252-4

85. Morgunova E, Taipale J. Structural perspective of cooperative transcription factor binding. *Curr Opin Struct Biol* 2017;**47**:1–8.
https://doi.org/10.1016/j.sbi.2017.03.006

86. Ibarra IL, Hollmann NM, Klaus B *et al*. Mechanistic insights into transcription factor cooperativity and its impact on protein–phenotype interactions. *Nat Commun* 2020;**11**:124.
https://doi.org/10.1038/s41467-019-13888-7

87. Gotthard G, Mous S, Weinert T *et al*. Capturing the blue-light activated state of the phot-LOV1 domain from Chlamydomonas reinhardtii using time-resolved serial synchrotron crystallography. *IUCrJ* 2024;**11**:792–808.
https://doi.org/10.1107/S2052252524005608

88. Alderson TR, Kay LE. NMR spectroscopy captures the essential role of dynamics in regulating biomolecular function. *Cell* 2021;**184**:577–95. https://doi.org/10.1016/j.cell.2020.12.034